Phase matching of high-order harmonics in a semi-infinite gas cell

Daniel S. Steingrube,* Tobias Vockerodt, Emilia Schulz, Uwe Morgner,† and Milutin Kovačev
Institut für Quantenoptik, Leibniz Universität Hannover, Welfengarten 1, D-30167 Hannover, Germany
and Centre for Quantum Engineering and Space-Time Research (QUEST), Hannover, Germany
(Received 19 August 2009; published 19 October 2009)

Phase matching of high-order harmonic generation is investigated experimentally for various parameters in a semi-infinite gas-cell (SIGC) geometry. The optimized harmonic yield is identified using two different noble gases (Xe and He) and its parameter dependence is studied in a systematic way. Beside the straightforward setup of the SIGC, this geometry promises a high photon flux due to a large interaction region. Moreover, since the experimental parameters within this cell are known accurately, direct comparison to simulations is performed. Spectral splitting and blueshift of high-order harmonics are observed.

DOI: 10.1103/PhysRevA.80.043819 PACS number(s): 42.65.Ky, 42.50.Nn

I. INTRODUCTION

Coherent vacuum-ultraviolet (vuv) radiation provided by high-order harmonics is a useful tool with applications to various fields of physics. For many applications a high photon flux at high photon energies is necessary, or at least beneficial. The atomic response of an atom in a strong laser field generating high-order harmonics is understood by the simple-man's model [1], or in a fully quantum-mechanical treatment by the Lewenstein model [2]. However, not only the single atomic response is important to the overall yield of high-order harmonics, but the macroscopic effects of phase matching play a major role.

High-order harmonics generation (HHG) is realized by different schemes employing gas jets [3], hollow waveguides [4], or gas cells [5]. The best investigated geometry regarding phase matching relies on focusing the fundamental laser pulse into a gas jet. Depending on the focus position, different phase-matching regimes can be realized optimizing, for example, the short electron trajectory [6] and allowing for attosecond pulse generation [7,8]. Beside the good understanding of the phase matching, this geometry holds several drawbacks for experimentalists. The estimate of the accurate gas density at the place of HHG for this scheme is difficult. Moreover, handling high pressure requires a pulsed gas jet to reduce the total gas flux. This, however, sets an upper limit for using jets at high repetition rates of the generating laser pulses.

In the present work, a semi-infinite gas-cell geometry [9,10] is applied for HHG. This scheme features a straightforward handling without the need for alignment of the laser to neither a gas jet nor entry and exit pinholes. The pressure at the place of HHG is known accurately, which provides the possibility for direct comparison of the experiment with simulations. Due to the large laser-gas-interaction region, this geometry promises a higher photon yield than in a gas jet configuration [5,11,12]. Since the phase-matching conditions of HHG in this geometry are not well investigated, a systematic study on experimental phase matching regarding focus position and gas pressure is performed for different focusing geometries. For our study, we use two different noble gases, xenon and helium. The former having a low ionization potential, and the latter a high ionization potential. The experimental results agree well with performed theoretical calculations. We investigate conditions for optimized generation of harmonics at high energies with possible application to attosecond pulse generation when using few-cycle pulses [13].

II. EXPERIMENTAL SETUP

Our experimental setup is sketched in Fig. 1. Experiments are performed using 35 fs pulses with 1.2 mJ at 785 nm central wavelength with a repetition rate of 3 kHz from a commercial chirped-pulse-amplifier system (Dragon, KM-Labs Inc.). These pulses are focused into the semi-infinite gas cell (SIGC), which consists of a gas-filled cell with entrance window, and exit pinhole (inlet in Fig. 1). The entrance window is far from the laser focus to avoid any nonlinear effects in the entrance area. Before an experiment, the fundamental beam drills the exit pinhole into an exchangeable metal plate allowing for straightforward handling and no further alignment procedures of the gas target. The diameter of the exit pinhole measures about 300–600 μm, depending on the chosen focal length, and serves as a differential pumping stage to ensure absorptionless propagation of the generated radiation in vacuum. The SIGC is filled with up to 20 mbar xenon, or up to 80 mbar helium, which is not an upper limit. Measurements were performed up to 267 mbar in argon [11], and we realized during our measurements pressure up to 250 mbar in helium.

The radiation is spectrally resolved by a monochromator setup (LHT 30, Horiba-Jobin-Yvon) using a toroidal grating (500 lines/mm). A multi-channel-plate detector with Chevron configuration detects the radiation. Finally, the detector signal is amplified by a lock-in amplifier and recorded by a computer.

III. SIMULATIONS ON PHASE MATCHING

Simulations are performed in a paraxial approximation assuming a Gaussian temporal and spatial profile of the fun-

*Corresponding author; steingrube@iqo.uni-hannover.de
†Also at Laser Zentrum Hannover e.V., Germany.

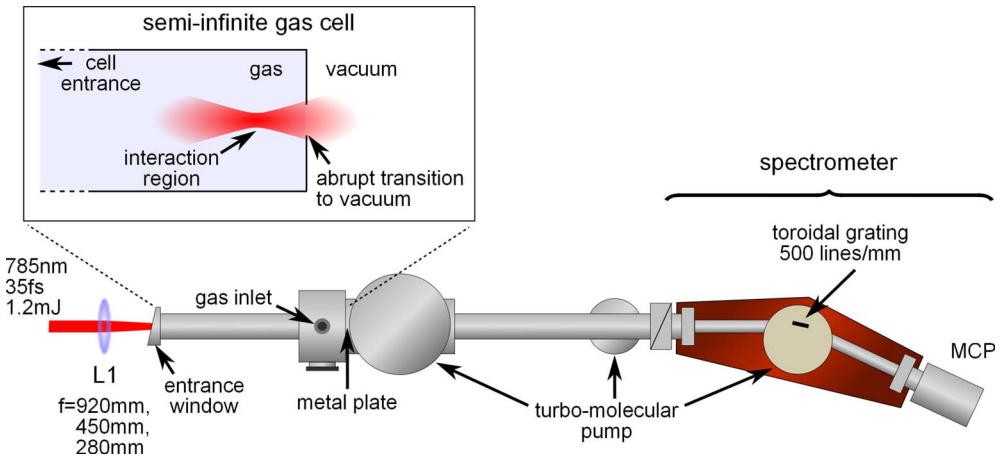

FIG. 1. (Color online) Experimental setup. The fundamental laser pulse is focused into the semi-infinite gas cell (see inlet) with a self-drilled pinhole exit. This abrupt transition to vacuum assures absorptionless propagation of the harmonic beam into the spectrometer.

damental laser field. According to [14], the far field at the detector plane (r',z') is computed for each harmonic q with wave vector k_q at the discrete harmonic frequency ω_q,

$$E_q(r',z',t') \sim k_q^2 \int dr dz \frac{P_q(r,z)\exp(-i\Delta\Phi_q)}{z-z'} \times \exp\left(\frac{ik_q}{2}\frac{r^2+r'^2}{z'-z}\right) J_0\left(\frac{k_q r r'}{z'-z}\right). \quad (1)$$

J_0 denotes the zero-order Bessel function, and $\Delta\Phi_q$ denotes the complex phase mismatch discussed below. The complex nonlinear polarization P_q is simulated using the Lewenstein model [2,15] with a hydrogenlike model for the dipole matrix element. The integration is performed from $z=-100$ mm, where harmonic generation is negligible, to the position z_f where the abrupt transition to vacuum is located. The radial coordinate is integrated from 0 to 200 μm, exceeding the beam waist by approximately a factor of 4.

Finally, the harmonic yield is integrated in the far field at $z'=1$ m according to

$$I_q \sim \int dr' dt' r' |E_q(r',z',t')|^2. \quad (2)$$

The radial coordinate r' is integrated from 0 to 100 μm. Details can be found in Ref. [14].

The complex phase mismatch is evaluated by the expression $\Delta\Phi_q = \int_{-\infty}^{z} dz'' \Delta k_q(z'') - i\int_{z}^{+\infty} dz'' \kappa_q(z'')$, where dispersion included in Δk_q and absorption (κ_q) of neutral atoms is computed via atomic scattering factors from [16]. Beside dispersion of neutral atoms and geometric effects [14], the phase-matching wave vector Δk_q includes contributions from free electrons [17] $\Delta k_{el,q} = (q^2-1)\omega_p^2/2c\omega_q$ with plasma frequency ω_p. The density of neutral atoms and free electrons is calculated applying the Ammosov-Delone-Krainov ionization rate [18]. Note that effects of nonlinear order, such as plasma defocusing [17], are not considered in the propagation of the fundamental field.

In our simulations, we use 30 fs pulses centered around 800 nm with pulse energies of 1.2 mJ for the driving laser field, which is comparable to our experimental conditions. Fine adjustment of the parameter as M^2, beam diameter D at the lens, and the focal length f, which are not known with high accuracy, are fitted to experimental data. Therefore, a standard genetic algorithm is applied evaluating the squared distance between peak intensities of simulation and experiment for selected harmonics versus focus position presented in the following section. Using the parameter $M^2=1.4$, $D=10.3$ mm, and $f=451$ mm, intensities up to 2.5×10^{15} W/cm^2 are reached.

IV. EXPERIMENTS

The harmonic intensity is investigated in dependence of the gas pressure and the focus position for several focal lengths (920, 450, and 280 mm). A short focal length of 150 mm did not lead to reliable results, which is presumably due to difficulties in controlling the pressure gradients at the exit pinhole during the measurement. Changing the z position of the lens in this condition is very critical since the laser carries still enough intensity for ablation beyond the confocal parameter enlarging the pinhole. Short focal lengths therefore affect the pressure conditions in the SIGC and present a limitation to the usage of this target geometry.

(a) Variation in the focus position. The position of the focus z_f relative to the exit of the SIGC is varied, as sketched in Fig. 2(a), by changing the position of lens L1. Figure 2(b) shows the harmonic peak spectral intensities versus harmonic order and focus position for a focal length of $f=450$ mm. It indicates that the optimum focus position for lower harmonic orders is slightly outside the gas cell [$z_f>0$, see Fig. 2(a)], whereas higher harmonic orders are generated within the cell $(z_f<0)$ most efficiently. In Figs. 2(c)–2(e), the normalized peak intensity of harmonics is plotted versus focus position, showing clearly this effect. The optimal yield of harmonic H19 is for a focus position at the exit pinhole $(z_f\approx0)$. In contrast, the maximum yield of harmonic H59 is at around −8 mm. Along with the experimental data, Figs. 2(c)–2(e) show results from the simulation, which are in reasonable agreement with the experimental data.

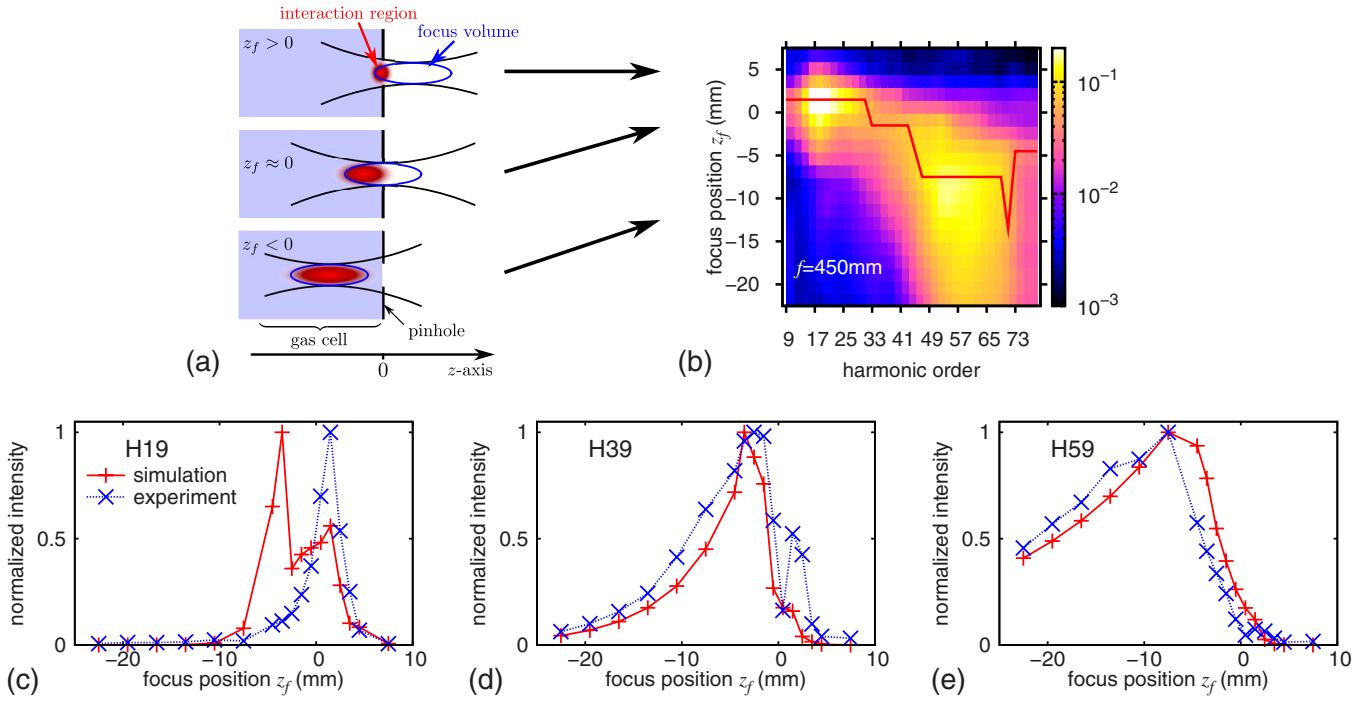

FIG. 2. (Color online) Variation in the focus position in 70 mbar helium for a lens with focal length of $f=450$ mm. (a) Sketch of the focus position relative to the gas cell with indication of the interaction region. At position $z_f=0$ mm, the focus is centered at the cell exit. Negative positions indicate that the focus is contained within the gas cell. The arrows indicate the positions of the three cases at subfigure (b). (b) Experimental harmonic peak intensities versus focus position on a logarithmic color (gray) scale. The red solid line shows the position of the maximum peak intensity of a harmonic (same for other presented maps in this paper). [(c)–(e)] Comparison between experiment ($\times$) and simulation (+) for different harmonic orders (as labeled).

The observation of the dependence of low and high harmonic orders on z_f is explained considering Fig. 2(a). Placing the focus outside the gas cell ($z_f>0$), only the lower peak intensity before the focus is within the interaction region where harmonic radiation is generated. Consequently, high orders cannot be generated. Moving the focus into the gas cell ($z_f<0$), it becomes possible to reach higher peak powers for the generation of harmonics of higher orders. The decrease in harmonic yield for lower orders is accounted mostly to reabsorption by the medium.

In vicinity of $z_f\approx 0$, there is a drop in the yield for all harmonic orders. This is explained considering the total phase of the nonlinear polarization, which shows strong variations at this position [6]. Consequently, the coherence length and, more general, the phase-matching conditions are deteriorated. Harmonics are therefore generated mainly before the focal spot, where phase-matching conditions allow for harmonic generation. Increasing z_f leads to an improvement of the harmonic yield, as the propagation length in the absorbing medium decreases for the harmonics generated before the focal spot.

On the other hand, harmonic emission originates mainly behind the focal spot, if the focus is placed inside the gas cell ($z_f<0$). Other contributions suffer absorption because of their long propagation distance to the gas-cell exit pinhole. As a result, the spatial origin of the harmonic radiation can be selected by variation in the focus position in the SIGC, leading to different phase-matching conditions.

(b) Different focal lengths. In Fig. 3(a), the phase-matching map of the harmonic yield versus focus position in 30 mbar helium is shown using a lens with 920 mm focal length. Due to a lower helium pressure than in Fig. 2(b), absorption effects are less pronounced and harmonics are generated over a large range of focus positions. Figure 3(b) shows the map for a lens with a focal length of 280 mm in 70 mbar helium. The observed qualitative behavior is basically the same and at a similar range compared to the map using a 450-mm-focusing lens shown in Fig. 2(b). The maximally reached peak intensity decreases with shorter focal length as can be seen from the color scale [see also Fig. 2(b)].

In order to estimate the range of z_f values, where phase matching is reached experimentally, we introduce a phase-matching range. The phase-matching range is defined as the width of the z_f range, where the harmonic intensity is beyond half of the peak intensity. Figure 3(c) shows the phase-matching range at 30 mbar and 70 mbar helium pressure for the 59th harmonic along with simulations. The focal length is varied using the same parameter as quoted in Sec. III with constant input power, analogous to the performed experiments. Due to absorption effects, the range is smaller for high pressure as pointed out for Fig. 3(a). Otherwise, the range does not vary significantly with a chosen focal length for the considered harmonic H59 in helium. This can be explained by the following argument. Observing the peak intensities versus focus position, the peak intensity decreases from the maximum exponentially moving the focus position into the SIGC due to absorption. Moving z_f outside the SIGC, the peak intensity is reduced rapidly due to the reduc-

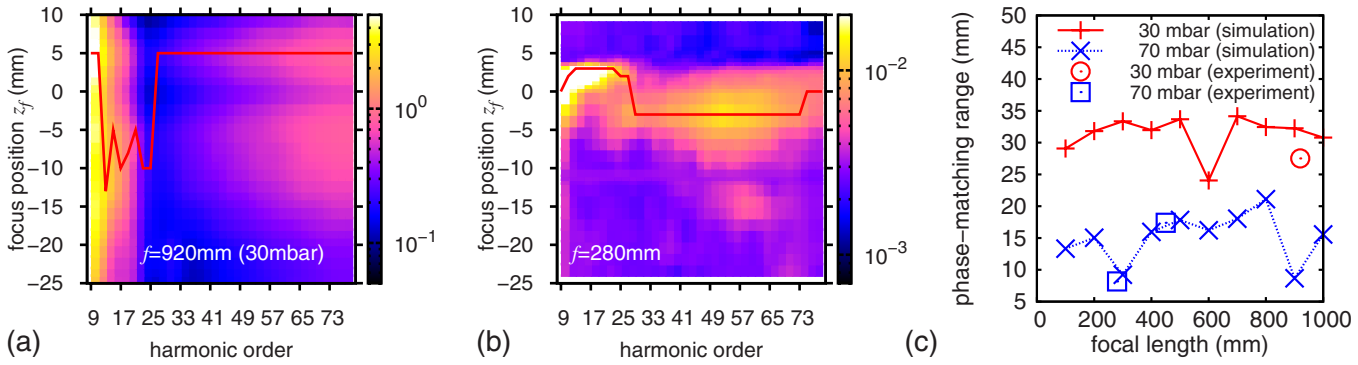

FIG. 3. (Color online) Variation in the focus position for different focal lengths: experimental harmonic peak intensities versus focus position on a logarithmic color (gray) scale for a focal length of (a) $f=920$ mm in 30 mbar helium and (b) $f=280$ mm in 70 mbar helium. See Fig. 2 for a focal length $f=450$ mm. (c) Phase-matching range (see text) of harmonic H59 versus focus position for 30 mbar and 70 mbar helium, respectively.

tion in the interaction volume. Because the second decay is very rapid and the decay due to absorption does not depend on the focal length, the phase-matching range remains more or less constant.

(c) Variation in the gas pressure. Leaving the focus position fixed at $z_f \approx 0$ mm, the helium gas pressure is varied from 5 to 80 mbar. We observe a monotonic increase in harmonic intensity with pressure [see Figs. 4(a)–4(c)]. At high pressure, a small saturation effect is observable for lower-order harmonics. The saturation effect can be accounted to absorption and is more relevant at lower harmonics in agreement with absorption data [16]. It is more pronounced using xenon as a generating medium (discussed below), as well as for harmonics H15–H23 generated in argon and presented in Ref. [11]. Higher harmonic orders in helium are not absorption limited in the considered pressure range, and the conversion efficiency can be further scaled even for focus positions within the SIGC. This remains valid even for high pressure measured up to 250 mbar for a lens with 280 mm focal length.

An excellent agreement between simulation and experiment is observable showing a similar increase in harmonic yield with saturation due to absorption. For low pressure, the expected p^2 dependency of phase-matched and absorptionless harmonic generation is shown as a solid line in Fig. 4.

(d) Xenon as generating medium. The harmonic peak intensity versus focus position using xenon, as a generating medium, is shown in Fig. 5. A similar dependence on the z_f position is observed, but the different phase-matching regimes are less pronounced compared to the helium case.

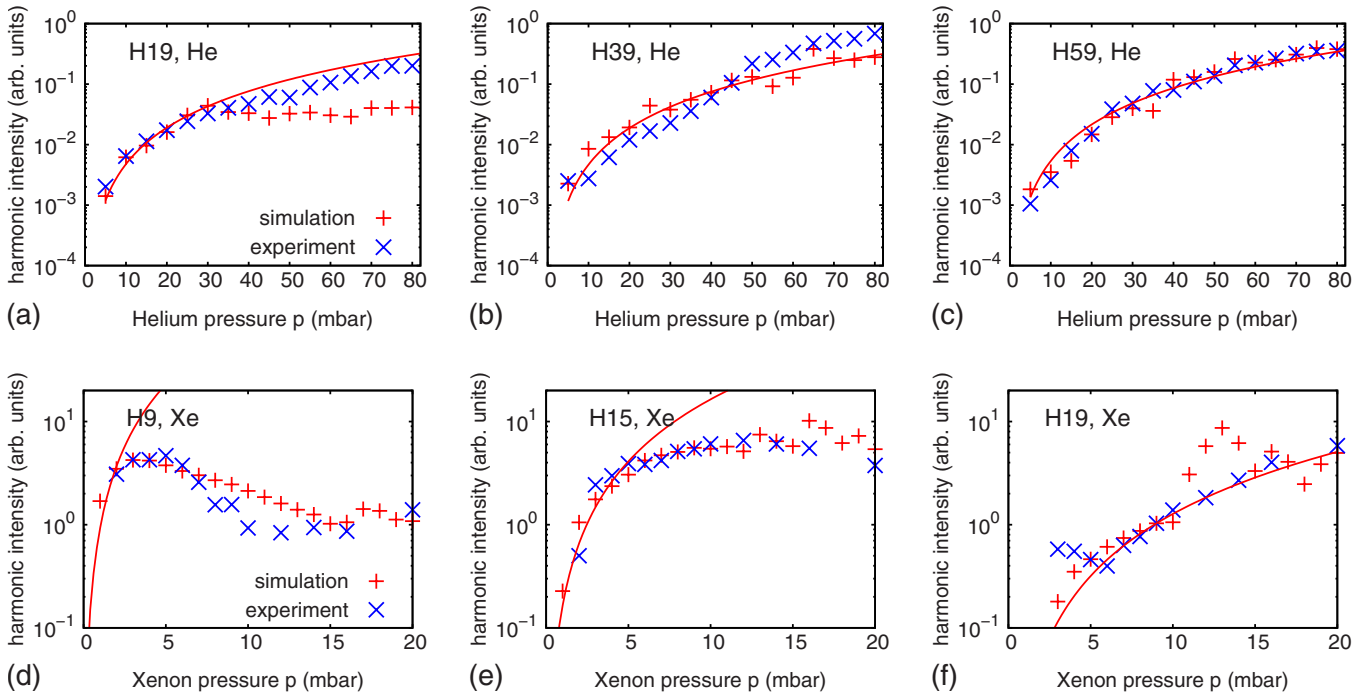

FIG. 4. (Color online) Experimental (×) and simulated (+) harmonic peak intensities versus [(a)–(c)] helium and [(d)–(f)] xenon gas pressure for different harmonic orders (labeled). The lens with 450 mm focal length is kept at a fixed position ($z_f \approx 0$). The solid line shows a fit for low pressure to a p^2 law.

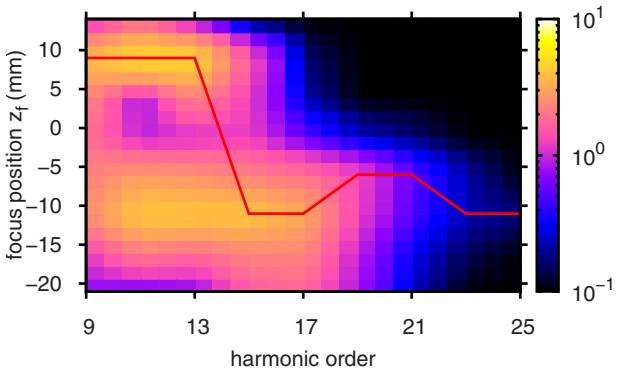

FIG. 5. (Color online) Variation in the focus position in 5 mbar xenon. Experimental harmonic peak intensities versus focus position for a lens with focus length $f=450$ mm on a logarithmic color (gray) scale. Note that the spectra are interpolated between harmonic orders and focus positions for better visualization.

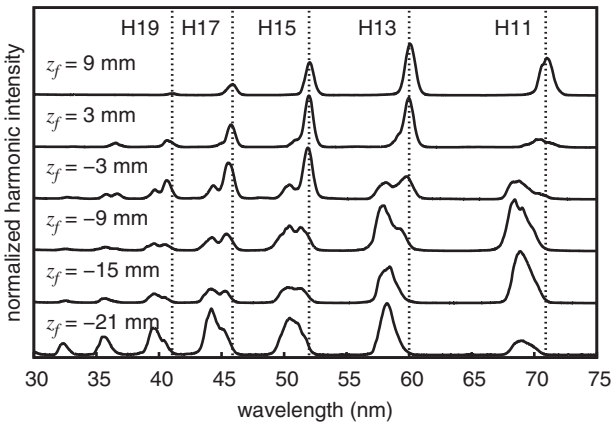

FIG. 6. Experimental results on variation in the focus position z_f in 5 mbar xenon using a 450-mm-focal-length lens. Blueshift and spectral splitting and broadening of the harmonics are visible.

Higher harmonics above H17 are generated only if the focus is contained within the gas cell for the same reasons as quoted previously [see Fig. 2(a)]. Since reabsorption of the generated radiation from xenon at lower pressure is negligible, the over-all harmonic yield does not decrease significantly compared to helium placing the focus far in the gas cell. However, increasing the xenon pressure, phase matching and absorption have a higher impact than in helium, as shown in Figs. 4(d)–4(f).

The xenon pressure is increased from 2 to 20 mbar resulting in a raising harmonic intensity for higher orders shown in Figs. 4(d)–4(f). We observe a saturation and even a decay in the harmonic peak intensity for lower orders (H9–H13) with increasing xenon pressure above ~6 mbar. This mainly results from absorption as quoted above for the case of helium. Increasing the interaction volume by moving the focus into the SIGC or using larger focal lengths, the saturation effect becomes more pronounced due to more absorption (not presented). The simulations shown in Figs. 4(d)–4(f) are in reasonable agreement with the experimental data confirming the saturation effect. However, a growing deviation between simulation and experiment can be observed with increasing pressure. This, on one hand, can be accounted to plasma defocusing of the fundamental [19], which is not considered in our simulations. On the other hand, the lower-order harmonics are affected by a large spectral broadening and splitting discussed below. This spectral splitting and broadening, however, result in a dramatic reduction in the spectral peak intensity. Since simulations are performed quasimonochromatically at a discrete harmonic frequency, these effects are intrinsically absent. At higher-order harmonics, the spectral broadening and splitting are less pronounced and simulations and experiments are matching.

(e) Spectral splitting, broadening, and blueshift. The effects of spectral splitting and broadening are shown in Figs. 6 and 7. Figure 6 shows the normalized harmonic spectrum generated in 5 mbar xenon for different focus positions. Splitting and broadening are hardly observable when the focus is placed outside of the SIGC ($z_f>0$), whereas it becomes stronger when moving the focus into the SIGC ($z_f<0$). Moreover, the harmonics are blueshifted for focus positions $z_f<0$, which is not present when the focus is outside the SIGC. These spectral effects are also dependent on pressure and pulse energy, as shown in Figs. 7(a)–7(c), respectively. With increasing pressure and pulse energy, all effects become more pronounced.

The reasons of the observed spectral blueshift, broadening, and splitting are discussed in literature controversially and is accounted to either a nonadiabatic [20–22] or an adiabatic effect [23–26]. The nonadiabatic effect is based on the time-dependent atomic phase for different trajectories in a rapidly changing pulse envelope. The adiabatic explanation considers macroscopic effects in a rapidly ionizing medium, which results in a blueshift of the fundamental, and a quasi-multi-pulse structure of harmonics due to temporally changing phase-matching conditions (transient phase matching). Due to the fact that there is a dependence of the effects on pressure and on focus position in our measurements, we attribute these effects to transient phase matching. Moreover, simulations on the adiabatic effect versus pressure [25] show very good agreement of the experimentally observed features visible in Fig. 7.

In the experiments using helium, the discussed spectral effects are hardly observable even at high pressure. Due to the high ionization potential of helium, the free-electron density is low and does not change much over the pulse. Thus, the effects are not much pronounced in contrast to xenon.

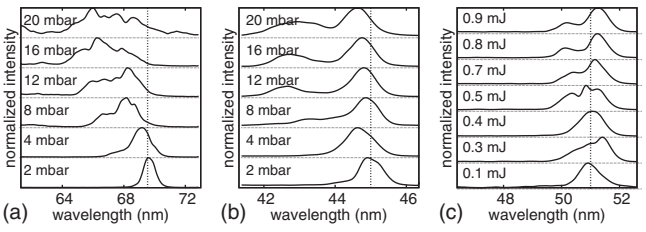

FIG. 7. Blueshift and spectral splitting and broadening of harmonics in xenon: dependence on pressure and pulse energy. Spectrum of harmonic (a) H11, and (b) H17 are shown at a fixed focus position ($z_f\approx0$ mm) for different pressure (450 mm lens). (c) Spectrum of harmonic H15 at a fixed position and pressure (−5 mm; 5 mbar) with varying pulse energy (280 mm lens).

V. CONCLUSION

We investigated the phase-matching conditions for a SIGC geometry experimentally. Harmonic spectra are observed, while focus position and gas pressure are varied systematically. This way, experimental phase-matching maps are generated in helium and xenon for lenses with different focal lengths. From these maps, phase-matching regions for specific harmonics can be extracted where the harmonic yield is optimized. Due to the benefits of an accurate knowledge of the pressure conditions within the SIGC, direct comparison between experiments and simulations yields an excellent agreement. Both experiment and simulation show that optimal phase-matching conditions for the generation of high-order harmonics in helium and xenon are reached when placing the focus position within the gas cell. A phase-matching range is introduced defining the range of focus positions where the harmonic signal is expected. This range is evaluated for harmonic H59 in helium and is found to depend only slightly on the chosen focal length.

Spectral splitting of single harmonics and blueshift is found to depend on pressure, focus position, and pulse energy. This indicates that these effects can be accounted to transient phase matching. We cannot confirm evidences for spectral splitting or blueshift due to nonadiabatic atomic responses in our experiments.

Reaching optimized conditions for high-order harmonic generation in a SIGC geometry will be important for high repetition rate ultrafast applications as, for example, the generation and exploration of attosecond pulses and the investigation of temporal dynamics on these electronic time scales.

ACKNOWLEDGMENTS

The authors like to thank Manfred Lein for reading the paper. This work was funded by Deutsche Forschungsgemeinschaft within the Cluster of Excellence QUEST, Centre for Quantum Engineering, and Space-Time Research.

[1] P. B. Corkum, Phys. Rev. Lett. **71**, 1994 (1993).
[2] M. Lewenstein, P. Balcou, M. Y. Ivanov, A. L'Huillier, and P. B. Corkum, Phys. Rev. A **49**, 2117 (1994).
[3] J.-F. Hergott, M. Kovacev, H. Merdji, C. Hubert, Y. Mairesse, E. Jean, P. Breger, P. Agostini, B. Carré, and P. Salières, Phys. Rev. A **66**, 021801(R) (2002).
[4] A. Rundquist, C. G. Durfee, Z. Chang, C. Herne, S. Backus, M. M. Murnane, and H. C. Kapteyn, Science **280**, 1412 (1998).
[5] E. Takahashi, Y. Nabekawa, and K. Midorikawa, Opt. Lett. **27**, 1920 (2002).
[6] P. Salières, A. L'Huillier, and M. Lewenstein, Phys. Rev. Lett. **74**, 3776 (1995).
[7] P. Antoine, A. L'Huillier, and M. Lewenstein, Phys. Rev. Lett. **77**, 1234 (1996).
[8] P. Agostini and L. F. DiMauro, Rep. Prog. Phys. **67**, 813 (2004).
[9] N. Papadogiannis, C. Kalpouzos, E. Goulielmakis, G. Nersisyan, D. Charalambidis, F. Augé, F. Weihe, and P. Balcou, Appl. Phys. B: Lasers Opt. **73**, 687 (2001).
[10] J. Peatross, J. R. Miller, K. R. Smith, S. E. Rhynard, and B. W. Pratt, J. Mod. Opt. **51**, 2675 (2004).
[11] J.-P. Brichta, M. C. H. Wong, J. B. Bertrand, H.-C. Bandulet, D. M. Rayner, and V. R. Bhardwaj, Phys. Rev. A **79**, 033404 (2009).
[12] J. C. Painter, M. Adams, N. Brimhall, E. Christensen, G. Giraud, N. Powers, M. Turner, M. Ware, and J. Peatross, Opt. Lett. **31**, 3471 (2006).
[13] D. S. Steingrube, E. Schulz, T. Binhammer, T. Vockerodt, U. Morgner, and M. Kovačev, Opt. Express **17**, 16177 (2009).
[14] A. L'Huillier, K. H. Schafer, and K. C. Kulander, J. Phys. B **24**, 3315 (1991).
[15] M. Lewenstein, P. Salières, and A. L'Huillier, Phys. Rev. A **52**, 4747 (1995).
[16] B. Henke, E. Gullikson, and J. Davis, At. Data Nucl. Data Tables **54**, 181 (1993); http://henke.lbl.gov/optical_constants/intro.html
[17] M. Bellini, C. Corsi, and M. C. Gambino, Phys. Rev. A **64**, 023411 (2001).
[18] M. V. Ammosov, N. B. Delone, and V. P. Krainov, Sov. Phys. JETP **64**, 1191 (1986).
[19] C. Altucci, T. Starczewski, E. Mevel, C.-G. Wahlström, B. Carré, and A. L'Huillier, J. Opt. Soc. Am. B **13**, 148 (1996).
[20] C. Kan, C. E. Capjack, R. Rankin, and N. H. Burnett, Phys. Rev. A **52**, R4336 (1995).
[21] H. J. Shin, D. G. Lee, Y. H. Cha, K. H. Hong, and C. H. Nam, Phys. Rev. Lett. **83**, 2544 (1999).
[22] E. Brunetti, R. Issac, and D. A. Jaroszynski, Phys. Rev. A **77**, 023422 (2008).
[23] C. Altucci *et al.*, Phys. Rev. A **61**, 021801(R) (1999).
[24] Y. Wang, Y. Liu, X. Yang, and Z. Xu, Phys. Rev. A **62**, 063806 (2000).
[25] F. Zhong, J. Deng, X. Hu, Z. Li, Z. Zhang, and Z. Xu, Phys. Lett. A **278**, 35 (2000).
[26] Zhong Fangchuan, Li Zhong, Zeng Zhinan, Zhang Zhengquan, Li Ruxin, and Xu Zhizhan, Phys. Rev. A **65**, 033808 (2002).